

Exploring complex phenomena using ultracold atoms in bichromatic lattices

Shuming Li¹, Indubala I Satija^{2,3}, Charles W. Clark³ and Ana Maria Rey¹

¹ *JILA, NIST, Department of Physics, University of Colorado, 440, UCB, Boulder, CO, 80309*

² *Department of Physics, George Mason University, Fairfax, VA, 22030, USA and*

³ *Joint Quantum Institute, National Institute of Standards and Technology and University of Maryland, Gaithersburg MD, 20899, USA*

(Dated: February 23, 2024)

With an underlying common theme of competing length scales, we study the many-body Schrödinger equation in a quasiperiodic potential and discuss its connection with the Kolmogorov-Arnold-Moser (KAM) problem of classical mechanics. We propose a possible visualization of such connection in experimentally accessible many-body observables. Those observables are useful probes for the three characteristic phases of the problem: the metallic, Anderson and band insulator phases. In addition, they exhibit fingerprints of non-linear phenomena such as Arnold tongues, bifurcations and devil's staircases. Our numerical treatment is complemented with a perturbative analysis which provides insight on the underlying physics. The perturbation theory approach is particularly useful in illuminating the distinction between the Anderson insulator and the band insulator phases in terms of paired sets of dimerized states.

PACS numbers: 03.75.Ss, 05.45.-a, 37.10.Jk

I. INTRODUCTION

Ultracold atoms are emerging as a versatile arena for the study of a variety of problems in physics. These clean and highly controllable systems can be viewed as simulators of complex quantum phenomena with applications in condensed matter, quantum optics, atomic and molecular physics and nonlinear dynamics, as well as in particle physics and cosmology [1, 2]. Some examples of this trend are the laboratory realization of the superfluid to Mott insulator transition with bosons [3], observation of the corresponding metal to Mott insulator transition with fermions [4, 5] and the creation of the Tonks-Girardeau gas in one dimensional systems [6, 7]. Ultracold atoms have also provided a laboratory realization of Wannier-Stark ladders [8] and the kicked-rotor model [9], a paradigm in the study of classical and quantum chaos [10]. Recent successful loading of atoms in a bichromatic optical lattice geometries [11], has opened new avenues for the study of phenomena where the competition between various length scales is at the heart of the problem.

Systems with competing lengths have fascinated physicists as well as mathematicians in view of their exotic fractal characteristics [12, 13]. Such systems with two competing periodicities, commonly known as almost-periodic or quasiperiodic, occur very commonly in nature. The most commonly studied example in quantum physics is the single particle Schrödinger equation in the presence of a quasiperiodic (QP) potential.

Motivated by experimental realization of two-color lattices, we revisit the problem of the Schrödinger equation in a quasiperiodic potential and its relationship with the Kolmogorov-Arnold-Moser (KAM) [14] problem of classical mechanics. Our particular focus is the treatment of many-body effects that are present in QP systems that have been extensively studied at the single-particle level. By focusing on experimentally accessible observables such as the momentum distribution and density-density correlations, we demonstrate the possibility of experimental visualization of the relationship between the metal-insulator transition and the KAM-Cantori transition [15] in many body systems. These observ-

ables are found to exhibit fingerprints of various paradigms of nonlinear systems such as Arnold tongues, bifurcations and devil's staircases. One of the aims of this paper is to communicate the excitement of ultracold atomic physics to the nonlinear dynamics community. We also hope that cold atom community will also benefit from our discussion of the relationship between problems of condensed matter theory and nonlinear dynamics.

The many-body systems that we treat here are ensembles of ultracold spin-polarized fermionic atoms confined in one-dimensional bichromatic optical lattices. We treat cases in which the two lattices have incommensurate periodicities, and thus constitute a quasi-periodic potential for atomic motion [16]. Since the metal-insulator transition in single-particle QP systems is associated with a localization transition of extended single-particle states, a natural probe of such transitions in many-particle systems are the density distribution and density-density correlations. At present, the density distribution of atoms confined in a lattice has not been easily accessible to experimental measurement, instead the quasi-momentum distribution and its corresponding correlation functions, have been measured after the lattice potential has been suddenly removed.

Using the momentum-position duality of our basic model [17, 18], we show that time of flight images encode local density information and can be used to identify the possible phases of ultracold atomic gases, e.g., metallic phases and various types of insulators. Many of our results are explained analytically using perturbation theory, although the complete picture is obtained by exact numerical calculations, particularly near the metal-Anderson insulator transition.

The paper is organized as follows. Section II contains an overview of experiments on ultracold atoms in optical lattices. Section III describes the basic Hamiltonian, and the experimental observables. In section IV, we describe the relationship between the metal-Anderson insulator transition and KAM-Cantori transition. In Section V we discuss possible experimental manifestations of effectively nonlinear behavior in these many-body systems. Sec. VI provides a summary of our

results and states our conclusions.

II. ULTRACOLD ATOMS IN OPTICAL LATTICES

An optical lattice is created by the interference of counter-propagating laser beams that give rise to a spatially periodic intensity pattern. The intensity pattern corresponds directly to a potential for neutral atoms via the a.c. Stark shift of the atomic energy levels. The two important parameters of an optical lattice are the depth of the lattice potential wells and the lattice constant, a . The well depth of the lattice can be tuned by changing the intensity of the laser, while a can be tuned by changing the wavelength of the laser or by changing the relative angle between the two laser beams [1].

The systems of interest here are gases of ultra-cold spin-polarized fermionic atoms trapped in the lowest band of a transversal 2D optical lattice. For most such systems of current experimental interest, where atomic interactions are short-range, spin-polarized fermions are effectively noninteracting due to Pauli blocking. The 2D lattice depth is made strong enough to freeze the motion of the atoms transversally, creating an array of independent 1D tubes [6, 19]. Along the axis of the 1D tubes, additional optical lattices can be imposed, as has been done in Refs. [7, 20]. We discuss cases in which two such lattices are imposed, with incommensurate periods [2] (when one of these lattices is much stronger than the other, we refer to it as the primary lattice). The combined lattices therefore generate an effective quasi-periodic (QP) potential along the axial direction. Such an experiment has been recently implemented for bosonic atoms in Ref. [11]. Our treatment considers cases where the ratio of the two lattice constants is equal to the “golden mean”, $\sigma = (\sqrt{5} - 1)/2$, which is one of the best-studied examples in single-particle physics [18].

In most experiments atoms are first trapped and cooled to quantum degeneracy. They are subsequently loaded into the lattice by adiabatically turning on the lattice laser beams. At the end of each experimental sequence atoms are probed by using time of flight images. These are obtained after releasing the atoms by turning off all the confinement potentials. The atomic cloud expands and then photographed after it enters the ballistic regime. Assuming that the atoms are noninteracting from the time of release, properties of the initial state can be inferred from the spatial images [21]: the column density distribution image reflects the initial quasi-momentum distribution, and the density fluctuations, namely the noise correlations, reflect the quasi-momentum fluctuations. These quantities, which will be defined below –see Eqs. (5,6)–, have been shown to be successful diagnostic tools for characterizing quantum phases and have been recently measured in bosonic quasi-periodic systems [22].

III. OUR MODEL SYSTEM: THE HARPER EQUATION, MANY-BODY OBSERVABLES AND SELF-DUALITY

A. The Harper Equation

If the intensity of the secondary lattice is much weaker than that of the primary lattice, the low energy physics of the fermionic system can be well described by the tight-binding Hamiltonian [2]:

$$H = -J \sum_j (\hat{c}_j^\dagger \hat{c}_{j+1} + \hat{c}_{j+1}^\dagger \hat{c}_j) + \sum_j V_j \hat{n}_j, \quad (1)$$

where \hat{c}_j is the fermionic annihilation operator at the lattice site j , and J is the hopping energy between adjacent sites. The main effect of the QP potential is to modulate the on site potential. It is accounted for by the term $V_j = 2V_0 \cos(2\pi\sigma j + \phi)$. The parameter V_0 is proportional to the intensity of the lasers used to create the secondary lattice [16], σ is the ratio between the wave vectors of the two lattices which we choose to take value $\sigma = (\sqrt{5} - 1)/2$, and ϕ is a phase factor that is determined by the absolute registration of the two lattices.

To model real experimental conditions, averaging over ϕ is required. This averaging takes into account, on one hand, the phase fluctuations from one preparation to another. Those arise due to the difficulty to lock the position of the cloud over several shots. On the other, the fact that typical experimental set-ups generally consist of an assembly of one-dimensional tubes with different lengths and phases among them.

For a single atom, the eigenfunctions $\psi_j^{(m)}$ and eigenenergies $E^{(m)}$ of the Hamiltonian in Eq.(1) satisfy:

$$-(\psi_{j+1}^{(m)} + \psi_{j-1}^{(m)}) + 2\lambda \cos(2\pi\sigma j + \phi) \psi_j^{(m)} = \epsilon^{(m)} \psi_j^{(m)}. \quad (2)$$

Where $\lambda = V_0/J$, $\epsilon^{(m)} = E^{(m)}/J$, and $\epsilon^{(m)} \leq \epsilon^{(m+1)}$. Eq. (2) is known as the Harper equation, a paradigm in the study of 1D quasiperiodic (QP) systems [18]. For irrational σ , the model exhibits a transition from extended to localized states at $\lambda_c = 1$. Below criticality, all the states are extended Bloch-like states characteristic of a periodic potential. Above criticality the Harper model becomes equivalent to a corresponding Anderson model, the spectrum is a pure point spectrum and all states are exponentially localized. At criticality the spectrum is a Cantor set and the gaps form a devil’s staircase of measure unity [12].

In our numerical studies, σ is approximated by the ratio of two Fibonacci numbers F_{M-1}/F_M , ($F_1 = F_0 = 1$, $F_{i+1} = F_i + F_{i-1}$), which describe the best rational approximant by continued fraction expansion of σ . For this rational approximation the unit cell has length F_M and the single-particle spectrum consists of F_M bands and $F_M - 1$ gaps. The gaps occur at $Q_n/2$, $\pm(\pi - |Q_n|/2)$ with $Q_n = \pm(2\pi/a)\langle n\sigma \rangle$ reciprocal lattice vectors constrained in the interval $aQ_n \in (-\pi, \pi]$. Here $\langle n\sigma \rangle = n\sigma \pmod{1}$, n an integer. We denote by N_p the number of atoms, $N_l = F_M$ is the number of lattice sites, and the filling factor $\nu = N_p/N_l$ ranges from 0 to 1.

B. Many-body Observables

An ensemble of spin-polarized fermions at zero temperature are “stacked up” into the single-particle eigenstates of increasing energy, with one particle per quantum state. The energy of the highest occupied level, which depends on the filling factor ν , is the Fermi energy, E_F . Since at the critical point all the single-particle wave functions become localized, at the many-body level polarized fermions also exhibit a transition from metal to insulator at λ_c . However, in addition to these two phases the fragmentation of the single-particle spectrum in a series of bands and gaps introduces additional band insulator phases when the Fermi energy lies within a gap. The most relevant insulating phases occur at the irrational filling factors: $\nu = F_{M-1}/F_M$ and $\nu = F_{M-2}/F_M$ (which respectively correspond to $\nu = \sigma, 1 - \sigma$), associated with the leading band gaps. In the band insulator phases the many body system is an insulator, irrespective of the value of λ , even though extended single particle states are occupied.

Since the metal-insulator transition is clearly signaled by the onset of localization of extended single-particle states, a natural probe of this transition is the many-body density profile, ρ_j , and the density-density correlations, $\Delta(j_1, j_2)$, which can be written in terms of single particle wave functions as:

$$\rho_j = \langle \hat{n}_j \rangle = \sum_{m=1}^{N_p} \left| \psi_j^{(m)} \right|^2 \quad (3)$$

$$\begin{aligned} \Delta(j_1, j_2) &= \langle \hat{n}_{j_1} \hat{n}_{j_2} \rangle - \langle \hat{n}_{j_1} \rangle \langle \hat{n}_{j_2} \rangle \\ &= \sum_{m=1}^{N_p} \left| \psi_{j_1}^{(m)} \right|^2 \delta_{j_1, j_2} - \left| \sum_{m=1}^{N_p} \psi_{j_1}^{(m)*} \psi_{j_2}^{(m)} \right|^2 \end{aligned} \quad (4)$$

Here $\hat{n}_j = \hat{c}_j^\dagger \hat{c}_j$ and we have used Wick’s theorem to evaluate $\Delta(j_1, j_2)$. However, in general, such local observables are hard to measure experimentally due to the lack of addressability of individual lattice sites for typical lattice spacing. Instead, time of flight images access non-local observables such as the quasi-momentum distribution, $\hat{n}(Q)$ and the quasi-momentum fluctuations, $\Delta(Q, Q')$, which are given by:

$$\hat{n}(Q) = \frac{1}{N_l} \sum_{i,j} e^{iQa(i-j)} \hat{c}_i^\dagger \hat{c}_j, \quad (5)$$

$$\Delta(Q, Q') = \langle \hat{n}(Q) \hat{n}(Q') \rangle - \langle \hat{n}(Q) \rangle \langle \hat{n}(Q') \rangle, \quad (6)$$

where Q is the quasi momentum which can be expressed in terms of the indices $k = 0, 1, 2, \dots$ as: $Q(k) = \frac{2\pi}{a} \frac{k}{N_l}$. $Q(k)$ is constrained to the interval $Qa \in (-\pi, \pi]$.

Introducing η_k , the Fourier transform of ψ_k ,

$$\eta_k^{(m)} = \frac{1}{\sqrt{N_l}} \sum_j e^{-i \frac{2\pi k j}{N_l}} \psi_j^{(m)}, \quad (7)$$

the observables n_k (also denoted sometimes as $n(Q(k))$) and

$\Delta(Q) \equiv \Delta(Q, 0)$ can be written as:

$$n_k = \sum_{m=1}^{N_p} \left| \eta_k^{(m)*} \eta_k^{(m)} \right|, \quad (8)$$

$$\Delta(Q(k)) = \sum_{m=1}^{N_p} \left| \eta_0^{(m)} \right|^2 \delta_{k,0} - \left| \sum_{m=1}^{N_p} \eta_k^{(m)*} \eta_0^{(m)} \right|^2. \quad (9)$$

C. Self-duality

The self-duality of the Harper equation corresponds to the property that single particle eigenstates ψ_j and their corresponding Fourier transformed eigenstates, $z_n \equiv \frac{1}{\sqrt{N_l}} e^{-in\phi} \sum \psi_j e^{-ij(2\pi\sigma n + \theta)}$ satisfy the same equation with the roles of J and V_0 interchanged [17, 18]:

$$-(z_{n-1} + z_{n+1}) + \frac{2}{\lambda} \cos(2\pi\sigma n + \theta) z_n = -\frac{\epsilon}{\lambda} z_n. \quad (10)$$

This relation implies that the experimentally relevant variables, η_k , (see Eq. (7)) also satisfy

$$\begin{aligned} &-(\eta_{\text{Mod}[k+F_{M-1}, F_M]} e^{-i\phi} + \eta_{\text{Mod}[k-F_{M-1}, F_M]} e^{i\phi}) \\ &+ \frac{2}{\lambda} \cos(2\pi k/F_M) \eta_k = -\frac{\epsilon}{\lambda} \eta_k \end{aligned} \quad (11)$$

As discussed below, self-duality is a key to obtaining experimental information on local quantities from measurements. In this context, it is important to understand the relationship between the index j of ψ_j that satisfies the Harper equation (2) and its corresponding index k in η_k that satisfies the dual equation (11). An example of the mapping is provided in Appendix A. It should be noted that Fibonacci sites in real space are mapped to Fibonacci sites in the momentum space, up to a common displacement. This shift is dependent on the phase factor ϕ . We obtain this relationship numerically by diagonalizing the Harper equation for a given λ , labeling the states in increasing order in energy, and then finding the corresponding momentum space dual by repeating the same procedure but with λ replaced by $1/\lambda$.

IV. LOCALIZATION TRANSITION AS A KAM-CANTORI TRANSITION

The perturbative treatment of the QP potential is fundamentally related to the treatment of a non-integrable perturbation applied to an integrable Hamiltonian system in classical mechanics. Both cases exhibit the small-divisors problem related to the presence of high-order terms with small denominators in the perturbation expansion. In the classical system, Kolmogorov, Arnold and Moser (KAM) [14] solved the problem and demonstrated that most of the invariant tori in the phase space are not destroyed by a sufficiently weak nonintegrable perturbation. Outside the perturbative regime, KAM tori break, becoming an invariant cantor set, known as Cantori [15].

The study of the Harper equation is fundamentally related to the KAM type problems of classical mechanics. Both systems share the mathematical difficulty of having higher-order terms with small denominators when the quasiperiodic potential or non-integrable term are treated perturbatively. Under this point of view, the metallic phase in the Harper Equation, with continuous spectrum and Bloch-type wave functions has been identified as the analog of the KAM phase with invariant tori, while the localized phase of the Harper system with point spectrum and exponentially localized states has been usually compared with the Cantori phase. At the single-particle level this connection has been visualized by means of the so called Hull function [23, 24] defined as $\psi_n = e^{in\alpha} \chi(n\sigma)$, with α a real phase factor. $\chi(n\sigma)$ is a smooth and continuous function in the extended phase but becomes discontinuous for $\lambda > 1$. Here we propose instead to look at the return map of the local density of the atomic cloud, ρ_j vs ρ_{j+1} , as a cleaner visualization of the KAM to Cantori transition at the many-body level.

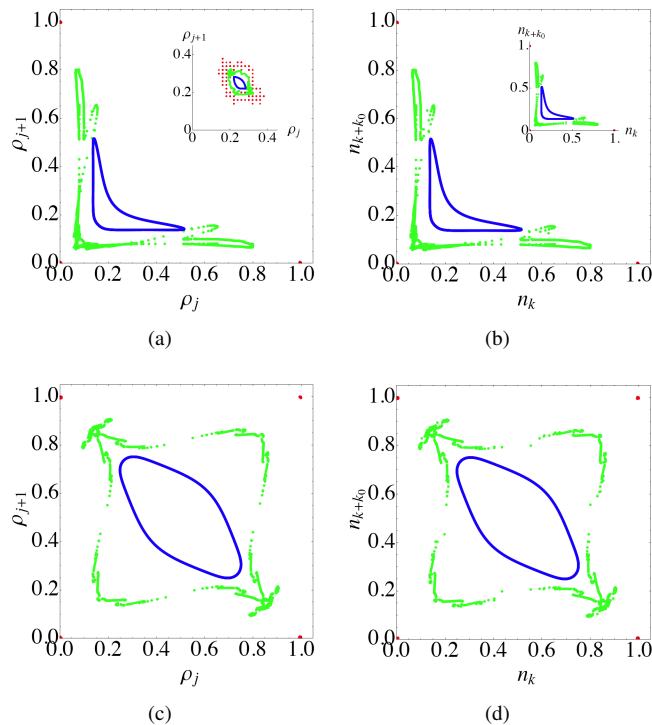


FIG. 1: (color online) Return maps in real space for (a) and (c) $\lambda = 10$ (red), 1(green), 0.5(blue) and the corresponding return map in momentum space (b) and (d) $\lambda = 0.1$ (red), 1(green), 2(blue). The filling factors are $\nu = 0.25$ for the upper panels and $\nu = 0.5$ for the lower panels. The insets are averaged over 50 random phases.

Fig.1 shows the return map for various rational filling factors $\nu = N_p/N_l = 1/4, 1/2$ and different values of λ . For $\lambda < 1$, the return maps are smooth curves and correspond to the KAM tori of the extended or metallic phase. For $\lambda > 1$, the density profile is a discontinuous function, a Cantori. The discreteness of the return map for generic filling factors can be easily understood in the $\lambda \rightarrow \infty$ limit, where the wave functions are fully localized and thus the return map can only

take the four possible values $(0, 0), (0, 1), (1, 0), (1, 1)$. Exactly at the transition point $\lambda = 1$, the smooth curves become disconnected.

Using the duality transformation, similar return maps can be drawn in momentum space, n_k vs $n_{k \pm k_0}$ ($k_0 = F_{M-1}$). While nearest neighbor sites are connected in position space due to a finite J , quasi-momentum components separated by the main reciprocal lattice vectors of the secondary lattice are connected by a finite V_0 . We find the momentum return maps exhibit an important advantage compared with the local density maps, which is related to the fact that they are insensitive to variations of the phase and retain their pattern when averaged over it. This is not the case in the density maps as shown in the insets of Fig. 1.

We now consider the case where the filling factor is a ratio of two main Fibonacci numbers ($\nu = \sigma, 1 - \sigma$). We refer to those filling factors as irrational filling factors since they approach an irrational number in the thermodynamical limit. As discussed earlier, this results in a band insulating phase as the Fermi energy E_F lies in the gap, just outside a filled band.

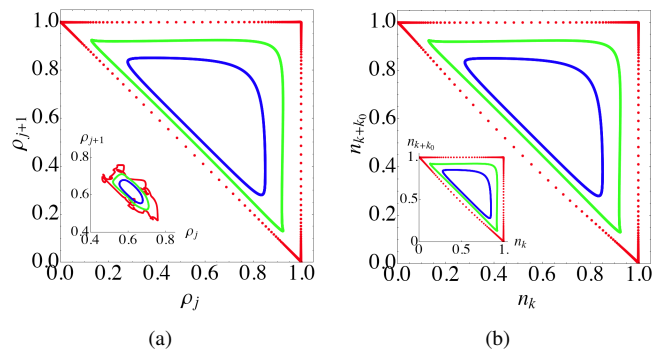


FIG. 2: (color online) Return maps for the irrational filling factor $\nu = \sigma$. Panel (a) is in real space with $\lambda = 10$ (red), 1(green), 0.5(blue) and panel (b) is in momentum space with the dual values $\lambda = 0.1$ (red), 1(green), 2(blue). The insets are averaged over 50 random phases.

In contrast to the generic or rational filling factors discussed earlier, the return map for the irrational filling case is found to remain smooth regardless of the value of λ (See Fig.2). This result may appear somewhat counterintuitive, because as $\lambda \rightarrow \infty$, all the single particle wave functions become localized. However, an exception to this simple picture occurs near irrational filling, when the density function exhibits a continuous distribution. This difference between the rational and the irrational filling is due to the presence of a group of paired states centered around the most dominant band edges (associated with the dominant gaps). Each of those states is dimerized, by which we mean that they localize at two neighboring sites. The existence of a pair of such dimerized states is the key to understanding the difference between rational and the irrational filling: although a single dimerized state causes delocalization near band filling (explaining irrational filling case), the existence of a pair can cancel the delocalization effect. Technical details of this argument are presented in Appendix B, where we show that the smooth character of the

map at the irrational fillings, σ, σ^2 associated with the leading gaps can be understood by the breakdown of non-degenerate perturbation theory in the large λ limit.

In summary, the band insulating phase belongs to the KAM phase irrespective of the strength of the disorder.

V. FINGERPRINTS OF NON-LINEAR PHENOMENA IN MANY-BODY OBSERVABLES

We now study the quasi-momentum distribution of polarized fermions, which is directly accessible in the time of flight images of ultracold atoms. In the following we will show how it imprints a signature of the KAM-Cantori transition and provides experimental realization of various landmarks of non-linear systems such as Arnold tongues and bifurcations.

A. Fragmented Fermi Sea

Fermions in the extended phase have metallic properties. For $\lambda = 0$, the single particle eigenstates are fully local-

ized in quasi-momentum space (and thus delocalized in position space) and $n(Q)$ is a step-like profile: $n(Q) = 1$ for $|Q| \leq Q_F$ and $n(Q) = 0$ for $|Q| > Q_F$ (Q_F is the Fermi momentum). For $0 < \lambda < 1$ the single particle eigenstates localized at k acquire some admixture of other quasi-momentum components ($n_{k \pm F_{M-1}}$ to leading order in λ). In this regime the quasi-momentum distribution retains part of the step-like profile but gets fragmented into additional structures centered at different reciprocal lattice vectors of the secondary lattice. We call the filled states centered around $Q = 0$ the main Fermi sea and those around the QP related reciprocal lattice vectors the quasi-Fermi seas.

The fragmentation of the quasi-momentum distribution and the development of QP Fermi seas can be understood from first order perturbation theory. To first order in λ the momentum landscape becomes fragmented in six regions, shown in Fig.3 and given by:

$$\tilde{n}_1 = \left(\frac{\lambda}{2}\right)^2 \frac{1}{4 \sin^2 \Theta \sin^2 (|Q|a - \Theta)} \quad (12)$$

$$\tilde{n}_2 = 1 - \left(\frac{\lambda}{2}\right)^2 \frac{1}{4 \sin^2 \Theta \sin^2 (|Q|a + \Theta)} \quad (13)$$

$$\tilde{n}_3 = \left(\frac{\lambda}{2}\right)^2 \frac{1}{4 \sin^2 \Theta} \left(\frac{1}{\sin^2 (|Q|a + \Theta)} + \frac{1}{\sin^2 (|Q|a - \Theta)} \right) \quad (14)$$

$$\tilde{n}_4 = 1 - \left(\frac{\lambda}{2}\right)^2 \frac{1}{4 \sin^2 \Theta} \left(\frac{1}{\sin^2 (|Q|a + \Theta)} + \frac{1}{\sin^2 (|Q|a - \Theta)} \right) \quad (15)$$

$$\tilde{n}_5 = 0 \quad (16)$$

$$\tilde{n}_6 = 1 \quad (17)$$

Where $\Theta = \frac{F_{M-2}}{F_M} \pi = \frac{|Q_1|a}{2}$. The various regions are delineated by the edges of the QP Fermi seas, shown by white lines in Fig.3 and given in the Q vs ν space by :

$$\nu = \frac{a}{\pi} |Q(k \pm \sigma N_l)| = \frac{a}{\pi} |Q(k \pm F_{M-1})| \quad (18)$$

The regions $\tilde{n}_{1,2}$, $\tilde{n}_{3,4}$ and $\tilde{n}_{5,6}$ reflect the characteristic particle-hole symmetry in fermionic systems.

As disorder is increased, more quasi-Fermi seas become visible, and with the increase of ν they overlap in a complicated pattern. Exactly at criticality, $\lambda = 1$, the pattern evolves into a fractal-like structure. Beyond the critical point, $\lambda > 1$, the fragmented quasi-momentum distribution profile disappears and instead it becomes a smooth function of Q and ν . This behavior is summarized in Fig. 4 and the corresponding cross sections for fixed Q and ν are displayed in Fig. 5 and Fig. 6.

At irrational filling factors, however, the quasi-momentum

distribution profile remains smooth regardless of the value of λ . The smoothness of the momentum distribution at these special filling factors can be understood using the same reasoning as the one used to understand the smooth character of the return map in position space in terms of non-degenerate perturbation theory. In this case, however, the states that are coupled are the ones localized at the quasi-momentum $Q_F + \epsilon_Q$ and $-Q_F + \epsilon_Q$, ($\epsilon_Q a \ll 1$).

The fragmentation of the Fermi sea in the $\lambda < 1$ regime, and the smooth profile in both the $\lambda > 1$ and band insulator

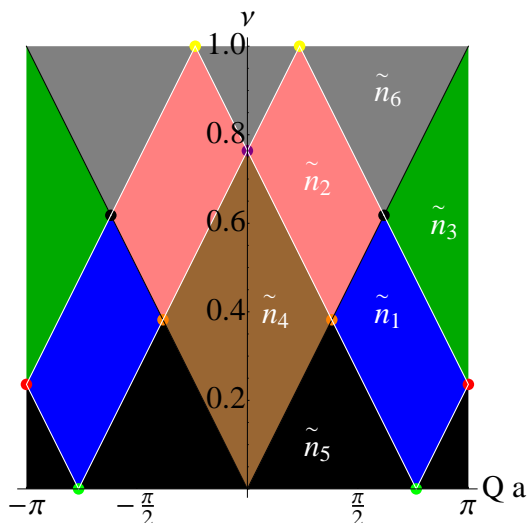


FIG. 3: (color online) Various boundaries of the fragmented Fermi sea.

phases are directly connected, via the self-duality property, to the discrete nature of the density return map in the localized phase, and its smooth character in the extended and band insulator phases.

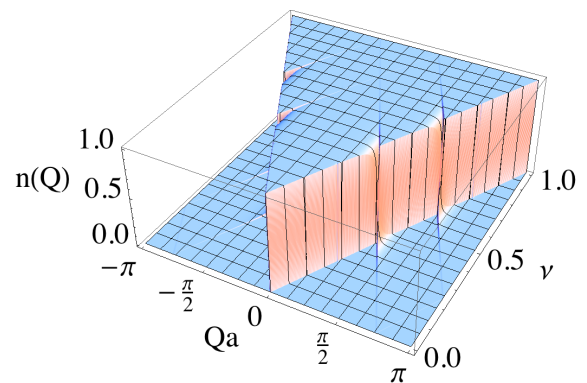
An important point to emphasize again, which is crucial for possible experimental observation of the predicted behavior, is the insensitivity of the momentum distribution to variations of the phase ϕ . We demonstrate such insensitivity by noticing that the quasi-momentum distributions plotted in Fig.4 are actually averaged over many different values of ϕ . Hereafter all the plots in momentum space are always averaged over 50 random phases.

B. Arnold Tongues

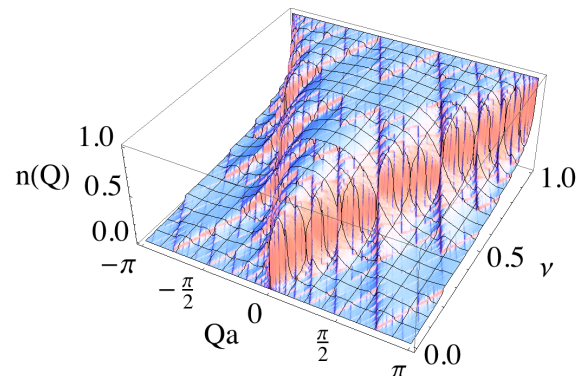
Arnold tongues are mode-locked windows that characterize the periodic dynamics of iconic non-linear systems with competing periodicities. In the 17th century Christian Huyghens [25] noted that two clocks hanging back to back on a wall tend to synchronize their motion. In general coupled systems such as coupled pendula or pendula whose lengths vary periodically with time exhibit mode-locking [26]. As the parameters of a system are varied, it passes through regimes that are mode-locked and regimes which are not.

Arnold-like Tongues also appear in the QP fermionic momentum distribution, where they reflect the complex nature of the physics induced by the competing periodicities.

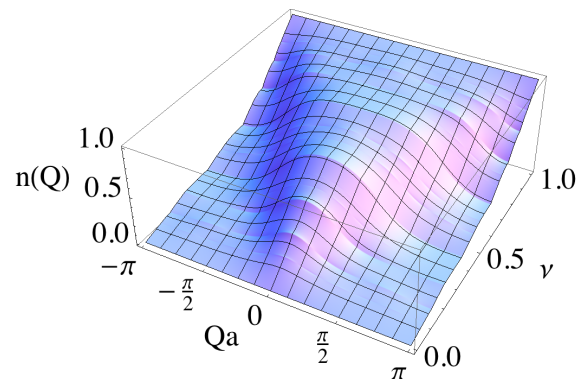
For $\lambda = 0$, the Fermi distribution is a binary distribution with only two values $n(Q) = 0, 1$. For finite λ and for generic filling factors, two windows of values centered around zero and unity become allowed whose width increases with λ as can be derived from a perturbative analysis. We call such windows QP tongues (See Fig. 7). Exactly at the onset of the metal-insulator transition the two distributions overlap, mimicking the Arnold tongue behavior. We have checked that the



(a)



(b)



(c)

FIG. 4: (color online) Momentum distribution for (a) $\lambda = 0.1$, (b) $\lambda = 1$, (c) $\lambda = 2$. All are averaged over 50 random phases to mimic a realistic experimental case. We can see that the sharp features of these distributions survive phase averaging.

duality of the Harper equation allows one to observe the formation of analogous structures in position space. The absence of a metal insulator transition at the irrational filling factors at which the system is a band insulator is also signaled by the disappearance of the Arnold tongues at these fillings, as shown in Fig. 7(b).

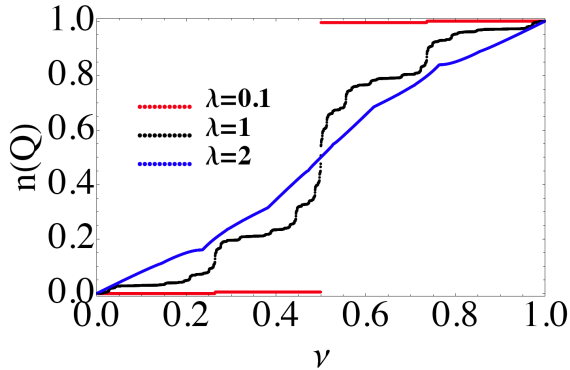


FIG. 5: (color online) Momentum distribution for fixed $Q(k = 1045)$, $F_M = 4181$ as a function of filling factors vs. the disorder parameter.

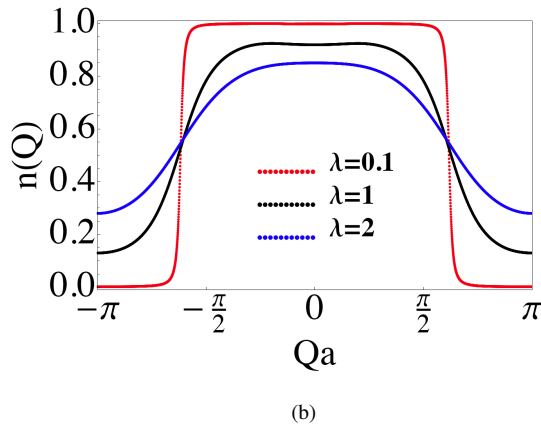
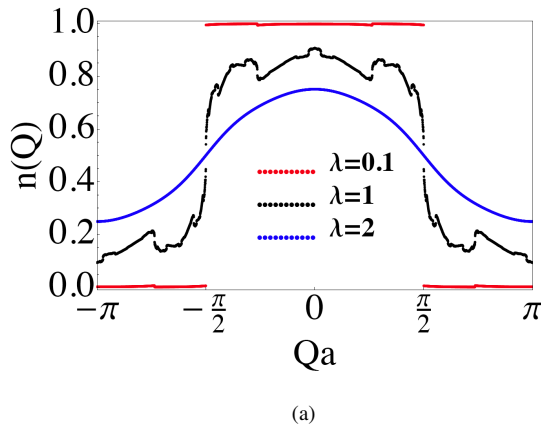


FIG. 6: (color online) Momentum distribution vs the disorder parameter. (a) $\nu = 0.5$, and (b) $\nu = F_{M-1}/F_M$.

C. Bifurcations

Bifurcations are common features observed in nonlinear dynamical systems, which occur when a small smooth change made to specific parameters (the bifurcation parameters) of

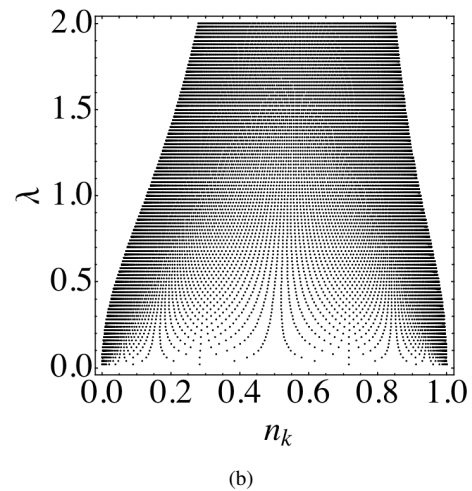
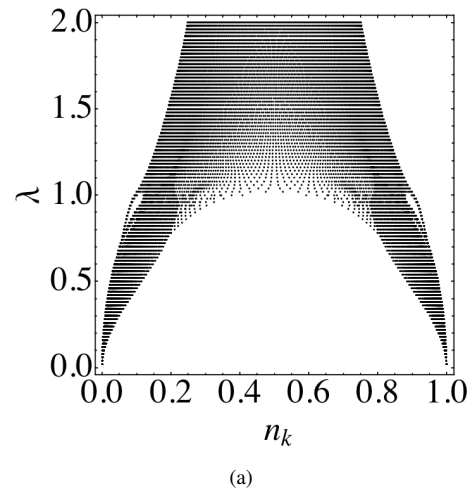


FIG. 7: Momentum distributions a function of disorder parameter. (a) filling factor $\nu = 0.5$. Here we see the formation of two Arnold tongues which merge at the critical value $\lambda = 1$. (b) $\nu = \sigma$. When ν is irrational, the system is a band insulator and no Arnold tongues are present. We have checked the existence of the similar structure in position space when converting λ to $1/\lambda$.

the system causes a sudden ‘qualitative’ or topological change in its behavior. A series of bifurcations can lead the system from order to chaos.

The density distribution provides a nice manifestation of a single bifurcation with λ as a bifurcation parameter. When the density at the various Fibonacci sites is plotted as a function of λ , for an specific filling factor which depends on the value of ϕ , a bifurcation opens up at $\lambda = 1$. In Fig. 8 the existence of a bifurcation at quarter filling ($\nu = 1/4$) when $\phi = 3\pi/4$ is shown.

A qualitative understanding of the bifurcation can be gained by considering the two limiting regimes, $\lambda \ll 1$ and $\lambda \gg 1$. In the weak coupling limit, $\lambda \ll 1$, the local density is uniform and directly proportional to the filling factor ν . On the other hand, in the strong coupling limit, a given site remains empty or occupied depending upon whether the onsite potential is

greater than or less than the Fermi energy.

Fibonacci sites $j = F_n$ have similar on-site energies which oscillate about $\epsilon_c \equiv 2\lambda \cos(\phi)$ (assuming $n \approx M$ and $\phi > 2\pi F_{M-n}/F_M$) as:

$$2\lambda \cos(2\pi\sigma F_n + \phi) = 2\lambda \cos(2\pi(-1)^{n-1} F_{M-n}/F_M + \phi) \begin{cases} < \epsilon_c & n \text{ is odd} \\ > \epsilon_c & n \text{ is even} \end{cases} \quad (19)$$

These oscillations can be seen in Fig.13 in Appendix A.

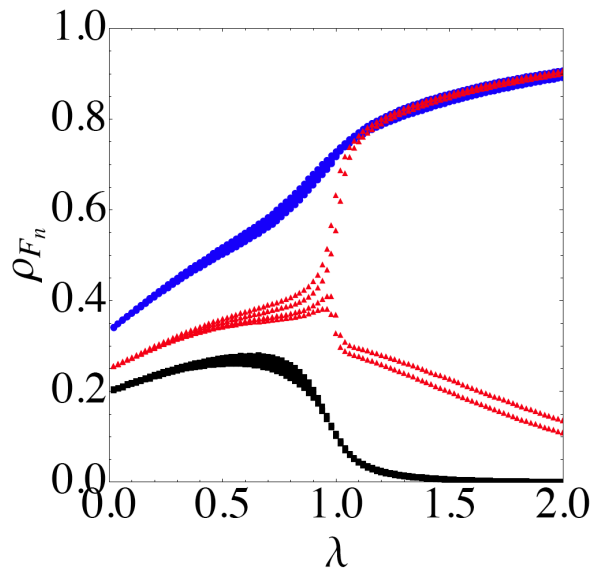
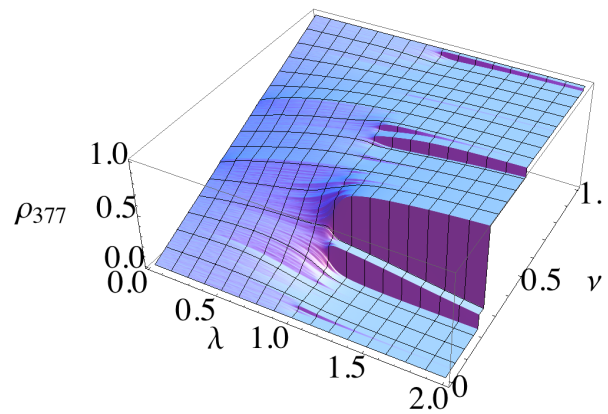


FIG. 8: (color online) Bifurcation of local density at Fibonacci sites. The central curve (red triangle) corresponds to quarter filling while the lowest (black blocks) and the topmost (blue disks) curves respectively correspond to $\nu = 1/5$ and $\nu = 1/3$. Quarter filling is a special case where the local density at Fibonacci sites is 0 or 1 as $\lambda \rightarrow \infty$. For $\nu > 0.25$, the Fibonacci sites are filled while for $\nu < 0.25$ Fibonacci sites are empty as $\lambda \rightarrow \infty$. We have checked the existence of the same bifurcation phenomena in the quasi-momentum distribution but with the weak and the strong coupling limits reversed ($\lambda \rightarrow 1/\lambda$).

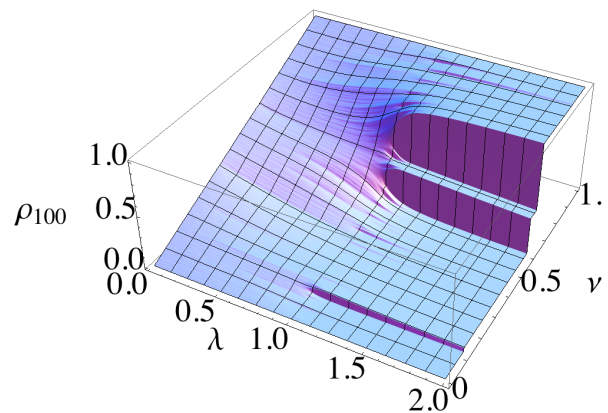
Consequently, at the filling factor, ν_c , at which the Fermi energy matches ϵ_c (e.g. if $\phi = 3\pi/4$ then $\nu_c \sim 0.25$) Eq. 19 implies that as λ goes to infinity, even Fibonacci sites (F_{2l}) become empty and odd Fibonacci sites (F_{2l+1}) become occupied. This behavior combined with the monotonic increase of the density with λ in the weak coupling limit qualitatively explains the observed bifurcation.

The self-dual behavior described by Eq.11 implies the existence of the same bifurcation phenomena in quasi-momentum distribution but with the weak and the strong coupling limits reversed ($\lambda \rightarrow 1/\lambda$).

When the local density is plotted for a generic lattice site as a function of λ and ν , the landscape shows a similar change in topology. In contrast to Fig. 8 where the filling factor is fixed but different curves corresponding to different Fibonacci sites



(a)



(b)

FIG. 9: (color online) Local density distribution as the disorder parameter and filling factor are varied for (a): Fibonacci site $j = 377$ and (b): normal site $j = 100$. We have checked the self-dual behavior in the quasi-momentum distribution with the weak and the strong coupling limits reversed ($\lambda \rightarrow 1/\lambda$).

are shown, in Fig. 9 the density at an specific lattice site is plotted but both the filling factor and disorder strength are varied. In this plot besides the large bifurcation there are smaller ones which cannot be explained by studying the two limiting cases. However, in momentum space they are qualitatively understood by considering cuts at a fixed λ as a function of ν . In these cuts the big jump at small λ can be identified with the edges of the main Fermi sea in the quasi-momentum profile

and the smaller jumps correspond to edges of the quasi-Fermi seas.

D. Devil's Staircases

A Devil's staircase describes a self similar function $f(x)$, with a hierarchy of jumps or steps. In other words, $f(x)$ exhibits more and more steps as one views the function at smaller and smaller length scale. The derivative of $f(x)$ vanishes almost everywhere, meaning there exists a set of points of measure 0 such that for all x outside it the derivative of $f(x)$ exists and is zero.

Cold atom experiments may provide an opportunity to visualize devil's staircases in the momentum-momentum correlations, namely the noise correlations.

Measurement of noise correlations is an example of Hanbury-Brown-Twiss interferometry (HBTI), which is sensitive to intrinsic quantum noise in intensity correlations. HBTI is emerging as one of the most important tools to provide information beyond that offered by standard momentum distribution-based characterization of phase coherence. The noise correlation pattern in 1D QP bosonic systems has been studied theoretically [27–30] and has also been measured experimentally [22]. Here however we focus on the fermionic system.

In the extended phase, noise correlations exhibit a series of plateaus as ν is varied, and the number of steps or plateaus increases as the strength of the disorder λ increases. The origin of this step-like structure with jumps occurring at the filling factors $\nu_{ju}^{(n)} = |Q_n|a/\pi$, can be understood from a perturbative argument as follows. For non-interacting fermions, for $Q \neq 0$ (See Fig.10), $\Delta(Q(k)) = -\sum_{m=1}^{N_p} \left| \eta_k^{(m)} \eta_0^{(m)} \right|^2$ with $\eta_k^{(m)}$ being the Fourier transform of the m^{th} single-particle eigenfunction. For $\lambda = 0$, the overlap between any two different Fourier components is always zero as only the ground ($m = 1$) state has a zero quasi-momentum component, i.e. $\eta_0^{(1)} = 1$. For small $\lambda \ll 1$, first order perturbation theory yields a single step observed at $\nu_{ju}^{(1)} = |Q_1|a/\pi$, as only $\eta_0^{(m^{(1)})}$ with $m^{(1)} = \nu_{ju}^{(1)} N_l$ is nonzero.

Quantitatively, the heights of the steps at $\nu_{ju}^{(1)}$ for $\lambda \ll 1$ are given by:

$$\begin{aligned} \zeta(0) &= -2 \left(\frac{\lambda}{2} \right)^2 \frac{1}{(1 - \cos(2\pi\sigma))^2} \\ \zeta(Q_1) &= \left(\frac{\lambda}{2} \right)^2 \frac{1}{(1 - \cos(2\pi\sigma))^2} \end{aligned} \quad (20)$$

Where $\zeta(0)$ ($\zeta(Q_1)$) is the step height for $\Delta(0)$ ($\Delta(Q_1)$) at filling factor $\nu_{ju}^{(1)}$. The minus sign implies a decrease in the noise as the filling factor ν increases. As λ increases, more and more steps are seen and can be explained using higher order perturbation theory. At criticality (see Figs.10-11), the steps acquire a hierarchical structure which resembles a devil's staircase and which correlates with the fractal

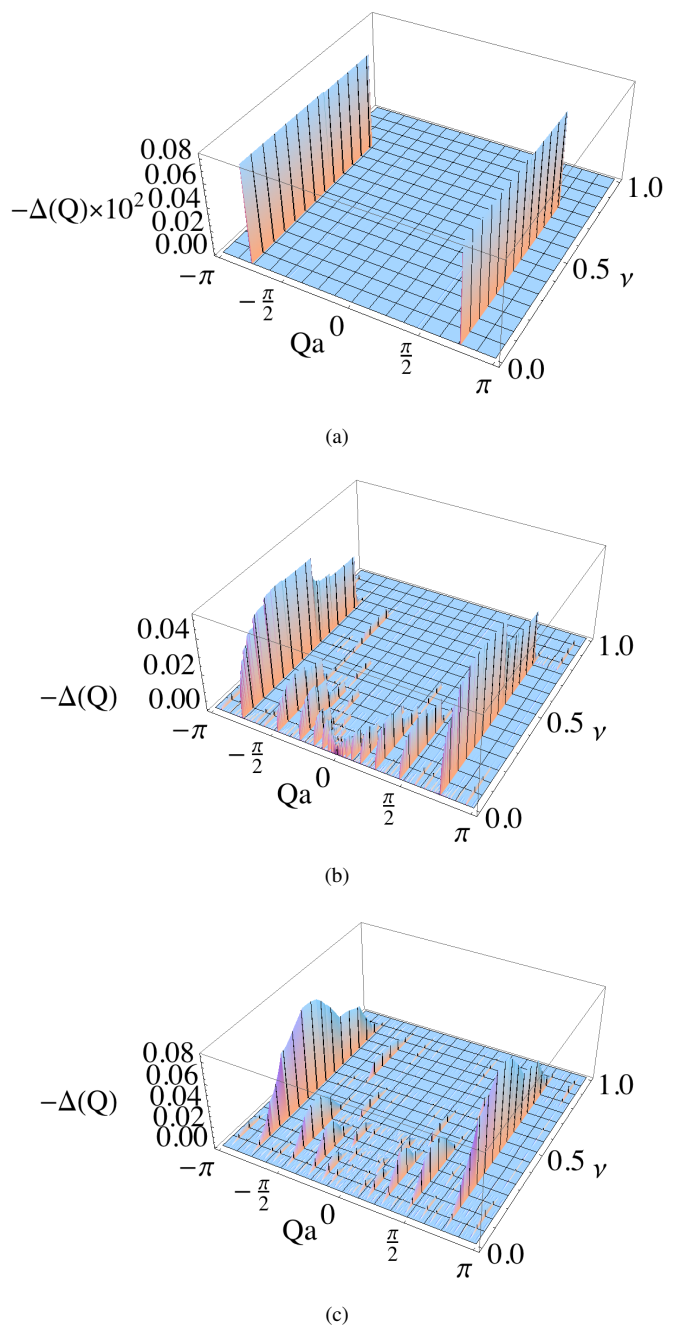


FIG. 10: (color online) Noise correlation for (a) $\lambda = 0.1$, (b) $\lambda = 1$, (c) $\lambda = 2$. All plots display averaged quantities over 50 random phases. We can see that structure in the noise correlations survives phase averaging, as for the momentum distributions of Fig. 4. $\Delta(Q = 0)$ is not displayed in those plots.

structure of the energy spectrum [23, 24]. In contrast to the momentum distribution, noise correlations do not show significant differences between the rational and irrational filling factors.

In the localized phase, $\lambda > 1$, we see the smoothing of the step-structure and the noise correlation function tends towards a sinusoidal profile $\Delta(Q_n) \approx \nu \delta_{n,0} - \frac{\sin^2(\pi \nu n)}{(\pi n)^2}$.

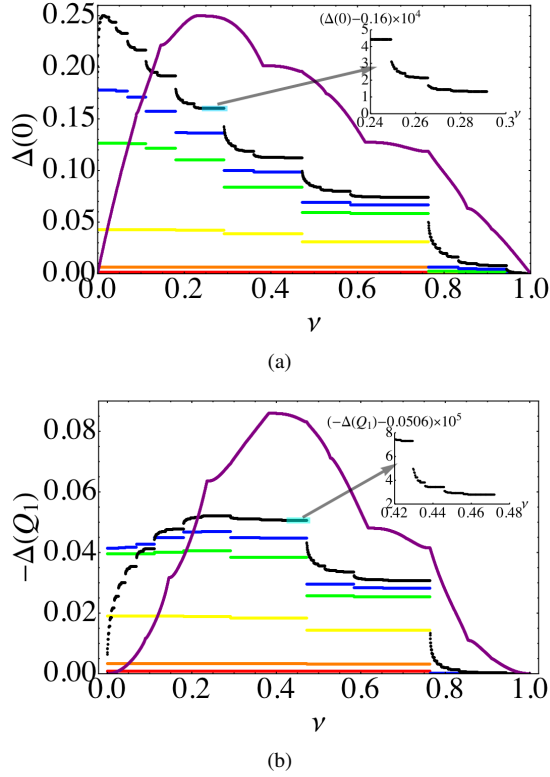


FIG. 11: (color online) This figure shows the evolution of $\Delta(Q_n)$ ($n = 0, 1$) as a function of the filling factor for different λ values. In the limit $\lambda \ll 1$, it exhibits steps occurring at the filling factors $\nu_{ju}^{(m)}$ ($m = 1, 2, \dots$) (see text). In the limit $\lambda \gg 1$, $\Delta(Q_n)$ acquires a sinusoidal profile. The inset shows the self-similar nature of the steps at $\lambda = 1$.

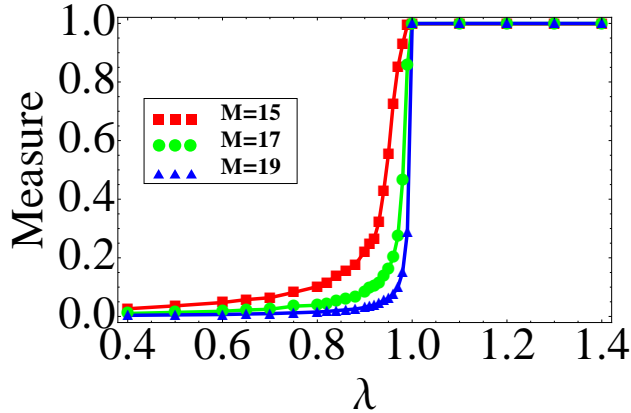


FIG. 12: (color online) This figure shows a measure of the gaps in $\Delta(0)$ vs λ for different system sizes, F_M . We deem that a gap occurs if $|\Delta(0)(N_p+1) - \Delta(0)(N_p)| > \epsilon$ (we choose $\epsilon = 10^{-15}$ here). We can see that with increasing M , the measure of the gaps approaches a step function with the step position at $\lambda = 1$.

To emphasize the striking difference between the noise patterns in the extended and localized phases (the step-like vs smooth profile), in Fig. 12 we plot a measure of the gaps developed in $\Delta(0)$ as a function of λ .

VI. SUMMARY

We now summarize our key results:

1. Extended-localized vs KAM-Cantori Phases

At the many-body level, the connection between the metal-insulator transition and the KAM-Cantori transition is signaled in the return map of the local density between nearest neighbor sites. For a given angle ϕ , the metallic phase with extended single particle wave functions exhibits a smooth return map. We identify this with the preserved invariant KAM tori in phase space at weak perturbations in the corresponding classical system. The localized phase displays a discrete return map, which we identify with the remaining tori or Cantori outside the perturbative regime. This behavior is shown in Fig.1. In addition, for the particular filling factors at which the system becomes a band insulator, the return map remains smooth for any value of λ (see Fig. 2).

Similar behavior can be observed in the corresponding momentum distribution return map. However, while the local density return map loses these characteristic features after averaging over ϕ , the momentum distribution return map remains almost unaffected. The robustness of the momentum return map to phase variations, is ideal for the experimental visualization of the metal-insulator vs KAM-Cantori connection in cold atoms.

2. Quasi-fractal structures and Arnold Tongues

The introduction of weak disorder modifies the characteristic step-function Fermi-sea profile of the quasi-momentum distribution. Additional step-function structures centered at different reciprocal lattice vectors of the QP lattice appear for $\lambda > 0$. We refer to those structures as the “quasi-Fermi seas”. With increasing λ and ν , the number and width of the various quasi-Fermi seas increase the fragmentation of the momentum distribution, turning it into a complex pattern. At $\lambda = 1$ the fragmentation becomes maximal and the momentum distribution evolves into a smooth profile as the system enters the localized phase (See figures 3-6). The overlap of the various quasi Fermi seas as one approaches criticality is reminiscent of the Arnold tongues overlap observed in non-linear systems, such as the circle map, as they enter the chaotic regime [31].

A more appropriate analogy of such behavior can be observed by considering the set of values taken by quasi-momentum distribution for a given filling factor. In the absence of disorder this distribution can only take

the values 1 or 0, depending upon whether the quasi-momentum is greater or smaller than the Fermi quasi-momentum. As the strength of the quasi-periodic lattice increases, two distributions of values develop, centered around 0 and 1 respectively. Their width increases with increasing disorder and they overlap exactly at criticality (Fig.7).

3. Bifurcations: The overlap between Arnold tongues at λ_c , can be linked, using the space-momentum duality transformation, to the appearance of a bifurcation in the density profile. The bifurcation occurs at a common but phase dependent filling for the various Fibonacci sites (Fig.8). At generic lattice sites, the filling factor at which the bifurcation takes place also depends on the lattice site under consideration and can be observed when the local density is plotted as a function of λ and ν (Fig.9).
4. Devil's staircases: Noise correlations plotted as a function of the filling factor exhibit step-like structures which evolve into a devil's staircase at the onset to the metal-insulator transition (figures 10-12).

Systems with competing periodicities stand in between periodic and random systems. The richness and complexity underlying such systems have been studied extensively [18]. Ultracold atoms are emerging as a promising candidate to simulate a wide variety of physical phenomena. Here we have shown they offer opportunities to experimentally realize various paradigms of nonlinear dynamics.

Our focus here was on spin-polarized fermionic systems, since we wanted to look at the simplest consequences of many-body physics in disordered systems. However, Bose-Einstein condensed systems may also be used as tools for laboratory investigation of various predictions made for the quasi-periodic systems based on single-particle arguments [16]. For example, it might be possible to confirm the strong coupling universality prediction, which establishes that the ratio of the single particle density at two consecutive Fibonacci sites should be a universal number [32].

Acknowledgments A. M. Rey and S. Li acknowledge support from the NSF-PFC grant and NIST.

Appendix A: Mapping from position to momentum space from self-duality relationship

Here we provide an example of the mapping between position coordinates j and quasi-momentum coordinates k which

we use to link the quasimomentum-position observables. In the plot we highlight the Fibonacci sites. A small system size is used to make the visualization clearer.

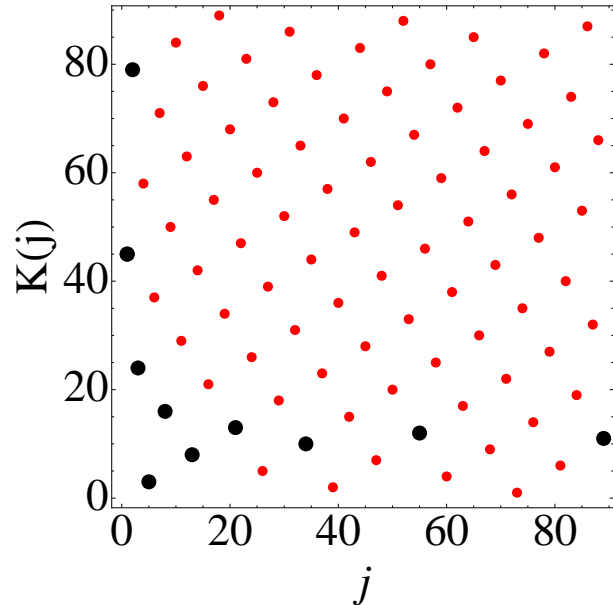


FIG. 13: (color online) Mapping from j to k used to determine momentum-space observables from position-space observables and vice versa. Larger points are Fibonacci sites. Here we choose $F_M = 87$, and $K(j)$ is the relation that maps j to k .

Appendix B: Perturbation Theory and Dimerized States

We begin our analysis with the Harper equation (2). For $\lambda \rightarrow \infty$, the single particle wave functions are localized at individual lattice sites, $\psi_j^{(m)} = \delta_{j,L_m}$ and $\epsilon^{(m)} = \cos(2\pi\sigma L_m + \phi)$, where L_m is defined by $\cos(2\pi\sigma L_{m-1} + \phi) \leq \cos(2\pi\sigma L_m + \phi)$. When $\lambda \gg 1$, we can get the single particle wave function through exact Diagonalization, or we can use the perturbation theory to obtain the approximate eigenvalues and eigenfunctions.

We focus first on the site L_m . Assuming that $2\lambda |\cos(2\pi\sigma L_m + \phi) - \cos(2\pi\sigma(L_m \pm 1) + \phi)| \gg 1$, non-degenerate perturbation theory can be used, and the results are:

$$\epsilon^{(m,0)} = 2\lambda \cos(2\pi\sigma L_m + \phi) \quad (\text{B1})$$

$$\epsilon^{(m,1)} = 0 \quad (\text{B2})$$

$$\epsilon^{(m,2)} = \frac{1}{2\lambda} \left(\frac{1}{\cos(2\pi\sigma L_m + \phi) - \cos(2\pi\sigma(L_m + 1) + \phi)} + \frac{1}{\cos(2\pi\sigma L_m + \phi) - \cos(2\pi\sigma(L_m - 1) + \phi)} \right) \quad (\text{B3})$$

$$\psi_j^{(m,0)} = \delta_{L_m, j} \quad (\text{B4})$$

$$\psi_j^{(m,1)} = -\frac{1}{2\lambda} \left(\frac{\delta_{L_m+1, j}}{\cos(2\pi\sigma L_m + \phi) - \cos(2\pi\sigma(L_m + 1) + \phi)} + \frac{\delta_{L_m-1, j}}{\cos(2\pi\sigma L_m + \phi) - \cos(2\pi\sigma(L_m - 1) + \phi)} \right) \quad (\text{B5})$$

where $\epsilon^{(m,0)}$, $\epsilon^{(m,1)}$, $\epsilon^{(m,2)}$ are the zeroth, first and second order terms of the eigenvalue $\epsilon^{(m)}$, with a similar meaning for $\psi_j^{(m,0)}$ and $\psi_j^{(m,1)}$. Also, $|\psi_j^{(m)}|^2 = \delta_{L_m, j} + O((\frac{1}{\lambda})^2)$. So, up to first order of $\frac{1}{\lambda}$, $\sum_j |\psi_j^{(m)}|^2 = 1$.

For other sites L_m that satisfy $1 \approx 2\lambda |\cos(2\pi\sigma L_m + \phi) -$

$\cos(2\pi\sigma(L_m + 1) + \phi)|$, non-degenerate perturbation theory doesn't work and degenerate perturbation theory will be used. In that case, the zero order energies ϵ and eigenfunctions ψ satisfy:

$$\begin{pmatrix} 2\lambda \cos(2\pi\sigma L_m + \phi) & -1 \\ -1 & 2\lambda \cos(2\pi\sigma(L_m + 1) + \phi) \end{pmatrix} \begin{pmatrix} \psi_{L_m}^{(m,0)} \\ \psi_{L_m+1}^{(m,0)} \end{pmatrix} = \epsilon \begin{pmatrix} \psi_{L_m}^{(m,0)} \\ \psi_{L_m+1}^{(m,0)} \end{pmatrix} \quad (\text{B6})$$

The above equations result in a pair of energies which we denote as ϵ_u and ϵ_d :

$$\epsilon_d = \lambda \{ \cos(2\pi\sigma L_m + \phi) + \cos(2\pi\sigma(L_m + 1) + \phi) \} - \sqrt{1 + \Lambda_m^2} \quad (\text{B7})$$

$$\epsilon_u = \lambda \{ \cos(2\pi\sigma L_m + \phi) + \cos(2\pi\sigma(L_m + 1) + \phi) \} + \sqrt{1 + \Lambda_m^2} \quad (\text{B8})$$

where $\Lambda_m = \lambda(\cos(2\pi\sigma L_m + \phi) - \cos(2\pi\sigma(L_m + 1) + \phi))$. The corresponding orthogonal eigenfunctions can be written as:

$$\psi_d = \begin{pmatrix} A \\ B \end{pmatrix} \quad \text{and} \quad \psi_u = \begin{pmatrix} B \\ -A \end{pmatrix} \quad (\text{B9})$$

where $A = \sqrt{\frac{\sqrt{\Lambda_m^2 + 1} - \Lambda_m}{2\sqrt{\Lambda_m^2 + 1}}}$, $B = \sqrt{\frac{\sqrt{\Lambda_m^2 + 1} + \Lambda_m}{2\sqrt{\Lambda_m^2 + 1}}}$. We can choose α (β) to be the greater (lesser) of A and B : $|\alpha|^2 = \frac{\sqrt{1 + \Lambda_m^2} + |\Lambda_m|}{2\sqrt{1 + \Lambda_m^2}}$, $|\beta|^2 = \frac{\sqrt{1 + \Lambda_m^2} - |\Lambda_m|}{2\sqrt{1 + \Lambda_m^2}}$. From these results one can see that $|\alpha|^2$ increases as $|\Lambda_m|$ increases. For example, when $|\Lambda_m| = 0$, $|\alpha|^2 = 0.5$ and when $|\Lambda_m| = \infty$, $|\alpha|^2 = 1$.

When $|\Lambda_m| \ll 1$, $|\beta|^2$ is comparable to $|\alpha|^2$ and the states are localized at the same two neighboring sites. Hence, they will be referred as a *pair of dimerized states* (The numerical results are shown in Fig.14 (a)). The dimerized states are found by noticing that:

$$\begin{aligned} & \cos(2\pi\sigma L_m + \phi) - \cos(2\pi\sigma(L_m + 1) + \phi) \\ &= 2 \sin(2\pi\sigma(L_m + 1/2) + \phi) \sin(\pi\sigma) \end{aligned} \quad (\text{B10})$$

So for the points that satisfy $|\sin(2\pi\sigma(L_m + \frac{1}{2}) + \phi)| \ll \frac{1}{\lambda}$, dimerized sites exist at L_m and $L_m + 1$. Since $\sigma = \frac{F_M - 1}{F_M}$,

it is clear that we can construct the relation $\text{Mod}[2\pi\sigma L_m + \phi, 2\pi] \approx 2\pi \text{Mod}[B_m/F_M, 1]$, where $m \in (1, 2, \dots, F_M)$ are indexes of increasing energy level, $L_m \in (1, 2, \dots, F_M)$ are indexes of sites' positions and $B_m = \text{Mod}[L_m \times F_{M-1} + l, F_M] \in (0, 1, 2, \dots, F_M - 1)$ are indexes that we introduce for the convenience of discussion (l is the closest integer to $\frac{\phi}{2\pi} F_M$). Using this relation it can be shown that $m \approx 2|B_m - F_M/2|$ (we use \approx here, since the exact expression for even and odd F_M are slightly different). The relations of m , L_m and B_m are plotted for the case of $F_M = 610$ in Fig.14 (b).

As we discussed, the dimerized states L_m satisfy:

$$\sin(2\pi\sigma(L_m + 1/2) + \phi) \approx 0 \quad (\text{B11})$$

Writing the above equation in terms of B_m , we get:

$$\sin\left(\frac{2\pi B_m}{F_M} + \pi\sigma\right) \approx 0.$$

The solutions are $\frac{2B_m + F_M - 1}{F_M} \approx 1$ or 2 . Therefore,

$$B_{m_1} \approx (F_M - F_{M-1})/2 \quad (\text{B12})$$

$$B_{m_2} \approx (2F_M - F_{M-1})/2 \quad (\text{B13})$$

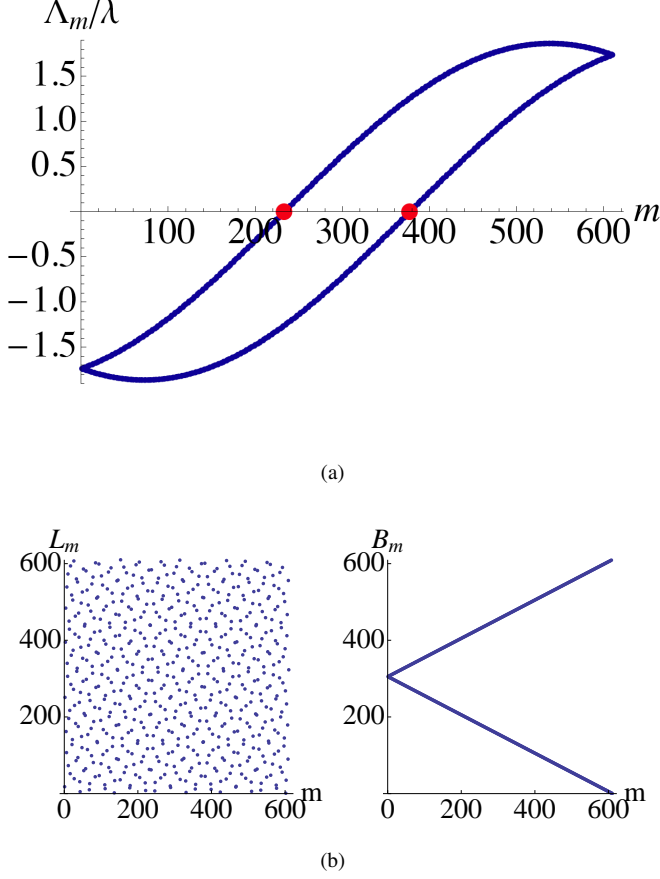


FIG. 14: (Color online): Panel (a) shows numerically that at the two red points, $m_1 = F_{M-1}$ and $m_2 = F_{M-2}$, Λ_m vanishes, so that degenerate perturbation theory is required. Panel (b) shows the relations of L_m , B_m and m (see text) for $\phi = \frac{3\pi}{4}$. The relations between L_m and m are very sensitive to the value of ϕ while the relations between B_m and m are not sensitive at all.

which correspond to:

$$m_1 \approx |2(B_{m_1} - F_{M/2})| \approx F_{M-1} \quad (\text{B14})$$

$$m_2 \approx |2(B_{m_2} - F_{M/2})| \approx F_{M-2} \quad (\text{B15})$$

A detailed analysis shows that the band opens exactly at $m_1 = F_{M-1}$ and $m_2 = F_{M-2}$ regardless of F_M being even or odd. This demonstrates, at perturbative level, the special behavior of the return map at irrational filling number F_{M-2} or F_{M-1} (See Fig.2).

In our calculations, we find out those L_m with the lowest values of $|\sin(2\pi\sigma(L_m + 1/2) + \phi)|$ (avoiding double counting of L_m in different pairs) and then apply to those points the perturbation theory we discussed above.

Based on the latter considerations it is possible to demonstrate that around $m_1 = F_{M-1}$ or $m_2 = F_{M-2}$, there exists a sequence of paired states, exhibiting the following relationships as $\lambda \rightarrow \infty$,

$$\begin{aligned} \psi_d^{i,\tau} &= \sqrt{A_i} \delta_{j, L_{m_\tau-i}} + \sqrt{1-A_i} \delta_{j, L_{m_\tau-i+1}} \\ \psi_u^{i,\tau} &= \sqrt{1-A_i} \delta_{j, L_{m_\tau-i}} - \sqrt{A_i} \delta_{j, L_{m_\tau-i+1}} \end{aligned}$$

with $i \ll F_M$ and $\tau = 1, 2$. These states determine the properties of the system when the Fermi energy is close to the major gaps, i.e. $\nu = \sigma$ or $\nu = \sigma^2$, and thus the main properties of the band insulator phases.

-
- [1] I. Bloch, J. Dalibard, and W. Zwerger, *Rev. Mod. Phys.* **80**, 885 (2008).
- [2] M. Lewenstein et al., *Advances in Physics* **56**, 243 (2007).
- [3] M. Greiner, O. Mandel, T. Esslinger, T. W. Hänsch, and I. Bloch, *Nature* **415**, 39 (2002).
- [4] R. Jördens, N. Strohmaier, K. Gunther, H. Moritz, and T. Esslinger, *Nature* **455**, 204 (2008).
- [5] U. Schneider et al., *Science* **322**, 1520 (2008).
- [6] T. Kinoshita, T. Wenger, and D. S. Weiss, *Science* **305**, 1125 (2004).
- [7] B. Paredes et al., *Nature* **429**, 277 (2004).
- [8] S. R. Wilkinson, C. F. Bharucha, K. W. Madison, Q. Niu, and M. G. Raizen, *Phys. Rev. Lett.* **76**, 4512 (1996).
- [9] F. L. Moore, J. C. Robinson, C. F. Bharucha, B. Sundaram, and M. G. Raizen, *Phys. Rev. Lett.* **75**, 4598 (1995).
- [10] F. L. Moore, J. C. Robinson, C. Bharucha, P. E. Williams, and M. G. Raizen, *Phys. Rev. Lett.* **73**, 2974 (1994).
- [11] L. Fallani, J. E. Lye, V. Guarrera, C. Fort, and M. Inguscio, *Phys. Rev. Lett.* **98**, 130404 (2007).
- [12] D. R. Hofstadter, *Phys. Rev. B* **14**, 2239 (1976).
- [13] M. Y. Azbel and M. Rubinstein, *Phys. Rev. B* **27**, 6530 (1983).
- [14] A. N. Kolmogorov, *Doklady Akad. Nauk SSSR* **93**, 763 (1953).
- [15] I. C. Percival, *Journal of Physics A: Mathematical and General* **12**, L57 (1979).
- [16] K. Drese and M. Holthaus, *Phys. Rev. Lett.* **78**, 2932 (1997).
- [17] S. Aubry and G. Andre, *Proceedings of the Israel Physical Society*, vol. 3 (Hilger, Bristol, 1979).
- [18] J. B. Sokoloff, *Physics Reports* **126**, 189 (1985).
- [19] B. L. Tolra et al., *Phys. Rev. Lett.* **92**, 190401 (2004).
- [20] C. D. Fertig et al., *Phys. Rev. Lett.* **94**, 120403 (2005).
- [21] E. Altman, E. Demler, and M. D. Lukin, *Phys. Rev. A* **70**, 013603 (2004).
- [22] V. Guarrera et al., *Phys. Rev. Lett.* **100**, 250403 (2008).
- [23] S. Ostlund and R. Pandit, *Phys. Rev. B* **29**, 1394 (1984).
- [24] S. Ostlund, R. Pandit, D. Rand, H. J. Schellnhuber, and E. D. Siggia, *Phys. Rev. Lett.* **50**, 1873 (1983).

- [25] B. van der Pol, Stated in a footnote in , *Philos. Mag.* **3**, 13 (1927).
- [26] V. I. Arnold, *Mathematical methods of classical mechanics, Chapter V* (Springer-Verlag, New York, 1994).
- [27] A. M. Rey, I. I. Satija, and C. W. Clark, *New Journal of Physics* **8**, 155 (2006).
- [28] A. M. Rey, I. I. Satija, and C. W. Clark, *Phys. Rev. A* **73**, 063610 (2006).
- [29] A. M. Rey, I. I. Satija, and C. W. Clark, *Laser Physics* **17**, 205 (2007).
- [30] T. Roscilde, *Phys. Rev. A* **77**, 063605 (2008).
- [31] E. Ott, *Chaos in Dynamical Systems* (Cambridge University Press, 1993).
- [32] J. A. Ketoja and I. I. Satija, *Phys Rev Lett* **75**, 2762 (1995).